Quasi-Two-Level PWM-Operated Modular Multilevel Converter With Nonlinear Branch Inductors

Jakub Kucka, *Member, IEEE*, Siqi Lin, Jens Friebe, *Member, IEEE*, and Axel Mertens, *Senior Member, IEEE*

***Abstract*—Quasi-two-level PWM operation of modular multilevel converters enables very low module capacitance even at low machine speeds and high torques while the current distortion is tolerable. In this article, the application of nonlinear inductors together with this operation mode is investigated to further decrease the module capacitances. The requirements for the inductors are analytically derived and the design of the nonlinear inductors using a stepped air gap is demonstrated. The feasibility and the advantages of quasi-two-level PWM operation with nonlinear inductors are validated using simulations and a laboratory prototype.**

***Index Terms*—Modular multilevel converter (MMC), nonlinear inductor, quasi-two-level.**

I. Introduction

THE modular multilevel converter (MMC), first presented in [2], offers many advantages, such as modularity, redundancy and fault tolerance, simple connection between the modules without the need for low inductive busbars, and a low total harmonic distortion (THD) output voltage that is changed only in small steps. If used in motor drive applications, the latter helps to reduce overvoltages at the motor terminals as well as bearing currents due to high-frequency (HF) common-mode currents [3]. The major disadvantage of MMCs is their high cost, which, to a large extent, can be attributed to the very large capacitors in each module. This inhibits the application of MMC in variable speed drives, if the base frequency of the motor is low and/or constant torque applications are targeted [4], [5].

Manuscript received July 16, 2020; revised October 19, 2020; accepted November 27, 2020. Date of publication December 9, 2020; date of current version March 5, 2021. This work was supported by the Deutsche Forschungsgemeinschaft (German Research Foundation) under Project 324166923. This article was presented in part at the 21st European Conference on Power Electronics and Applications, Magazzini del Cotone Conference Centre, Genova, Italy, September 2019. Recommended for publication by Associate Editor Z. Li. *(Corresponding author: Jens Friebe.)*

Jakub Kucka was with the Institute for Drive Systems and Power Electronics, Leibniz University Hannover, 30167 Hannover, Germany. He is now with the Power Electronics Laboratory, EPFL, 1015 Lausanne, Switzerland (e-mail: jakub.kucka@epfl.ch).

Siqi Lin, Jens Friebe, and Axel Mertens are with the Institute for Drive Systems and Power Electronics, Leibniz University Hannover, 30167 Hannover, Germany (e-mail: siqi.lin@ial.uni-hannover.de; friebe@ial.uni-hannover.de; mertens@ial.uni-hannover.de).

Color versions of one or more figures in this article are available at https://doi.org/10.1109/TPEL.2020.3042635.

Digital Object Identifier 10.1109/TPEL.2020.3042635

In such high-torque low-frequency drive applications, it is very desirable to reduce the necessary module capacitance. This can be achieved using quasi-two-level PWM operation of the MMC [6]–[8] that proved to reduce the installed module capacitance by more than one order of magnitude compared to conventionally operated MMCs [8]–[10]. The staircase trapezoidal voltage waveform of quasi-two-level PWM operation results in the same desirable properties as for the MMC output waveform, except that the output voltage and current distortion approach those of a two-level converter with the same PWM carrier frequency. However, unlike in HVDC applications, in most large drives, a PWM frequency of around 1 kHz results in a tolerable current THD. In summary, quasi-two-level PWM operation trades off the acceptably worse current THD against the significantly decreased requirements for the installed module capacitance, whereas all other advantages of MMCs are preserved.

Recently, an improved current control for the quasi-two-level PWM operation of MMC has been proposed in [9]. Increasing the output voltage range by making use of common-mode voltages and discontinuous modulation, as common for two-level inverters, was studied in [10]. Note that the control approaches for quasi-two-level PWM operation, which simplify the operation mode, proposed in [11] and [12], both apply significantly higher module capacitances and, thus, are not investigated in this article.

In the past, similar considerations as mentioned earlier led to the proposal of quasi-two-level PWM operation for neutral-point clamped multilevel converters [13], [14]. In modular converters, quasi-two-level operation was first presented for modular high-voltage dc–dc converters [15]–[17]. Furthermore, a quasi-two-level and quasi-three-level operation modes of MMC, at first glance similar to the one used in this article, were presented in [18] and [19]. However, there is a major difference. The operation modes from Diab *et al.* [18] and Wei *et al.* [19] do not control the leg currents of the converter, which leads to either significant branch current overshoots or likely higher values of the required capacitances [20].

This article is based on the particular quasi-two-level PWM operation of MMC, as described in [8]–[10]. References [8] and [10] showed that the energy that has to be buffered in module capacitors is approximately proportional to the energy stored in branch inductors of MMC. Consequently, reducing the

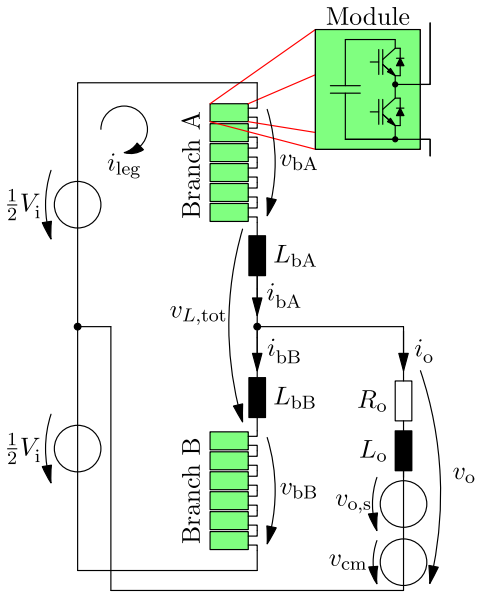

Fig. 1. Phase-leg model of an MMC.

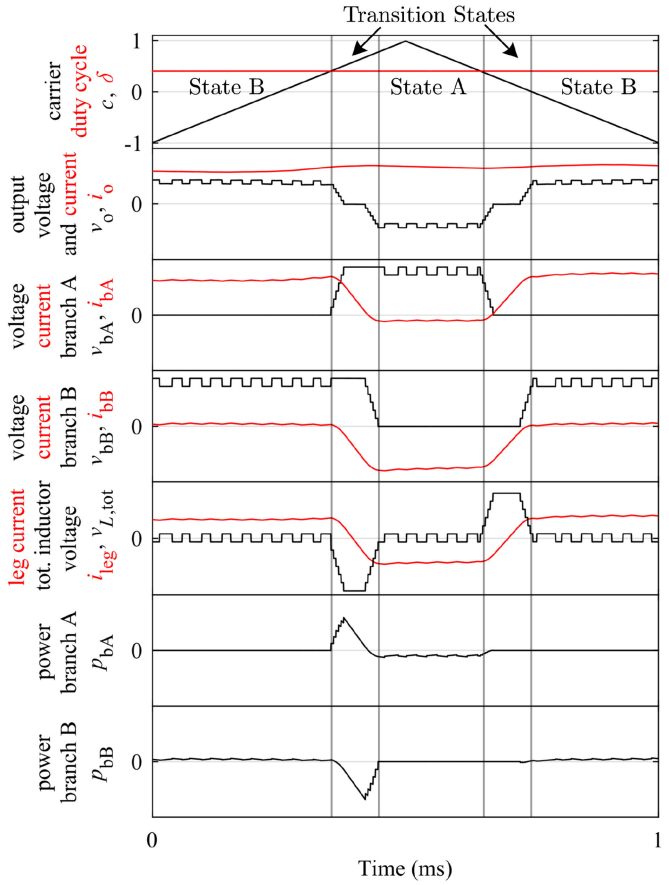

Fig. 2. Waveforms showing the concept of the quasi-two-level PWM operation mode over one PWM period ($f_{\mathrm{PWM}} = 1$ kHz) for positive currents and positive duty cycles. Linear branch inductors [$L_{\mathrm{bA}}(i) = L_{\mathrm{bB}}(i) = \overline{L}_{\mathrm{b}}$] are assumed and the MMC parameters are chosen to clearly show the various effects of the operation mode.

energy stored in branch inductors is expected to also reduce the necessary size of module capacitors. The energy stored in branch inductors can generally be reduced by an application of nonlinear saturable inductors in branches while the same branch-current ripple is maintained. This option is studied and validated in this article.

Note that the branch inductor coupling, such as in [21] and [22], leads to very similar converter behavior as standard non-coupled linear inductors without any impact on the sizing of the module capacitors but only on the inductor itself. Thus, it will not be further discussed in this article.

This article is structured as follows. First, the general operation principle of quasi-two-level PWM-operated MMCs is explained in Section II. Afterward, the novel idea is presented briefly in Section III and the desired characteristic of the nonlinear inductors is derived and specified in Section IV. Section V shows the design process of the specified nonlinear inductors and validates it using finite element method (FEM) simulations. A downscaled demonstrator prototype of the inductor is presented in Section VI and the necessary control adjustments in Section VII. Sections VIII and IX show the improvements achieved with the designed nonlinear inductors based on simulations and low-voltage experiments, respectively. Finally, the conclusion is drawn in Section X.

II. Operation Principle

The operation principle proposed in [9] can be explained for a single phase leg of MMC, depicted in Fig. 1, using the (somewhat exaggerated) waveforms from Fig. 2. A common-mode voltage v_{cm} is a result of the superposition of the output voltages for the particular phase legs (considering a typical three-phase MMC).

As can be seen in Fig. 2, the branch voltages are determined by PWM, by comparing the carrier c with the setpoint duty cycle $\delta \in [-\delta_{\max}, \delta_{\max}]$. Three possible states can be observed in Fig. 2, which are as follows.

1) State A: Branch voltage v_{bA} is high and branch voltage v_{bB} is zero. Hence, the output voltage v_{o} is negative.
2) State B: Branch voltage v_{bB} is high and branch voltage v_{bA} is zero. Hence, the output voltage v_{o} is positive.
3) Transition state: Either all modules are inserted (v_{bA} and v_{bB} are both high) or all modules are short-circuited (v_{bA} and v_{bB} are both zero). Hence, the output voltage v_{o} is approximately zero and the voltage drop over the branch inductors $v_{L,\mathrm{tot}}$ is maximized.

Since the modules are switched one by one with a switching delay T_{d} between two switching instants, the branch voltages and (consequently) the output voltage have a staircase trapezoidal waveform, which limits the $\mathrm{d}v/\mathrm{d}t$ of large voltage steps in the output voltage. The particular value of the worst-case $\mathrm{d}v/\mathrm{d}t$ can be adjusted by the delay value T_{d}.

The main idea of the operation mode is to adjust the leg current

$$i_{\mathrm{leg}} = \frac{1}{2} \cdot (i_{\mathrm{bA}} + i_{\mathrm{bB}}) \tag{1}$$

such that the branch currents i_{bA} and i_{bB} are low during states A and B, respectively. Consequently, the branch powers p_{bA} and p_{bB} are very low as well and the module capacitance can be reduced compared to that of the conventionally operated MMCs.

Between states A and B, transition states are applied to change the leg current as fast as possible. As can be seen in Fig. 2, the branch currents and the branch voltages can have nonzero values during transition state. Hence, power peaks are generated in branch powers p_{bA} and p_{bB} of the respective branches A and B. To compensate for these short-time power peaks, a low-magnitude power in opposite direction is generated in Branch A during state A and in Branch B during state B by the corresponding branch currents. As a consequence, the branch energy (representing the total energy stored in module capacitors of a single branch) is reset within each PWM period, making the energy pulsation in the modules very low and independent of the output frequency.

The desired value of the branch current during states A and B is set by a dead-beat closed-loop controller using a HF modulation visible at the branch voltages. Note that the HF modulation is expected to impact the switching losses only marginally, since the branch currents are low in magnitude when it is active. Further details regarding the operation principle and the control implementation can be found in [8] and [9].

III. Brief Introduction of the Novel Idea

As discussed in [8] and [10], there are contradictory requirements on the inductance value of the branch inductors. On the one hand, the branch inductance should have a high value during states A and B, so that the leg-current and branch-current ripples are low without the necessity for an exceedingly high HF modulation frequency. On the other hand, the branch inductances should be sufficiently low during transition state, to reduce its duration as much as possible and to lower the branch-energy disturbances ($\Delta e_{\mathrm{b}} \approx L_{\mathrm{b}} \cdot i_{\mathrm{o}}^2$ according to [8] and [10]), which determine the module capacitance.

Although a tradeoff between these two requirements for the branch inductance value has to be made when linear branch inductors with a constant inductance are used ($L_{\mathrm{bA}}(i) = L_{\mathrm{bB}}(i) = \overline{L}_{\mathrm{b}}$), an optimized behavior could be achieved with nonlinear branch inductors. The idea is that the branch inductor has a high inductance when the branch currents are low in magnitude, thus providing sufficiently high inductance during state A ($L_{\mathrm{bA}} = L_{\mathrm{b,max}}$) and state B ($L_{\mathrm{bB}} = L_{\mathrm{b,max}}$). When the branch currents are both high in magnitude during the transition state, both branch inductors have a very low inductance ($L_{\mathrm{bA}} = L_{\mathrm{b,min}}$, $L_{\mathrm{bB}} = L_{\mathrm{b,min}}$). Thus, the leg current can be changed faster and the duration of the transition state can be decreased, which leads to lower energy variation and smaller required module capacitances.

In the following section, the specifications for the nonlinear branch inductors are derived and the influences of the design parameters are discussed. Note that all inductances in this article are defined as differential (small-signal inductances).

IV. Specification of the Nonlinear Branch Inductor

A straightforward idea for the specification of the nonlinear branch inductor is depicted in Fig. 3(a). While the branch currents are low, the branch inductance has the value of $L_{\mathrm{b}}(i_{\mathrm{b}}) = L_{\mathrm{b,max}}$. Once the branch current reaches the value $I_{\mathrm{b,1}}$, the branch inductance drops instantaneously to $L_{\mathrm{b}}(i_{\mathrm{b}}) = L_{\mathrm{b,min}}$, enabling a faster change of the leg current. The switch-over value $I_{\mathrm{b,1}}$ can be determined in the way that the maximum branch current value of branch current $\max(i_{\mathrm{bA}}) \leq I_{\mathrm{b,1}}$ during state A and the maximum branch current value $\max(i_{\mathrm{bB}}) \leq I_{\mathrm{b,1}}$ during state B.

As can be derived from Fig. 1, the ripple of the leg current (as well as branch currents) depends on the sum of the inductance values $L_{\mathrm{bA}} + L_{\mathrm{bB}}$. Hence, in order to obtain the same worst-case leg-current ripple during states A and B as with two linear branch inductors with a constant inductance $\overline{L}_{\mathrm{b}}$, the sum of the inductances has to be identical during states A and B

$$L_{\mathrm{b,A}} + L_{\mathrm{b,B}} = 2 \cdot \overline{L}_{\mathrm{b}}. \tag{2}$$

Since one of the inductances is low ($L_{\mathrm{b,min}}$) and one of the inductances is high ($L_{\mathrm{b,max}}$) during states A and B, the sum of the minimum and maximum value of the branch inductance has to be

$$L_{\mathrm{b,min}} + L_{\mathrm{b,max}} = 2 \cdot \overline{L}_{\mathrm{b}} \tag{3}$$

in order to achieve the same worst-case ripple. The value $L_{\mathrm{b,min}}$ should be selected to be as low as possible to enable fast transitions with low branch energy disturbances but sufficiently high to limit the leg current's $\mathrm{d}i/\mathrm{d}t$ during transition states and fault conditions to a value manageable by the current controller. The manageable $\mathrm{d}i/\mathrm{d}t$ is mainly determined by the bandwidth of the current measurement and time delays within the controller.

The main issue with this straightforward branch-inductance characteristic from Fig. 3(a) can be recognized by looking at the output voltage equation derived from Fig. 1

$$v_{\mathrm{o}} = \frac{(L_{\mathrm{bB}} - L_{\mathrm{bA}}) \cdot \frac{1}{2} \cdot V_{\mathrm{i}}}{L_{\mathrm{bA}} + L_{\mathrm{bB}}} - \frac{L_{\mathrm{bA}} \cdot v_{\mathrm{bB}} - L_{\mathrm{bB}} \cdot v_{\mathrm{bA}}}{L_{\mathrm{bA}} + L_{\mathrm{bB}}}. \tag{4}$$

The equation states that the output voltage changes with the branch inductances. Consequently, if the branch inductances change instantaneously, the $\mathrm{d}v/\mathrm{d}t$ of the output voltage approaches infinity and the one of the advantages of the quasi-two-level PWM operation is diminished. These rapid changes in the output voltage are highlighted in the example simulated waveforms plotted in Fig. 3(c) near 0.46 and 0.56 ms. Therefore, the inductance value has to change continuously between the values $L_{\mathrm{b,max}}$ and $L_{\mathrm{b,min}}$ in order to limit the $\mathrm{d}v/\mathrm{d}t$ of the output voltage to acceptable levels. In the following paragraphs, a branch inductance characteristic is derived that leads to a continuous waveform of the output voltage during transition state with a constant gradient $\mathrm{d}v_{\mathrm{o}}/\mathrm{d}t$.

The fastest branch current (and thus the branch inductance) changes occur during the transition state. Hence, $v_{\mathrm{bA}} \approx V_{\mathrm{i}}$ and $v_{\mathrm{bB}} \approx V_{\mathrm{i}}$ can be substituted into the output voltage

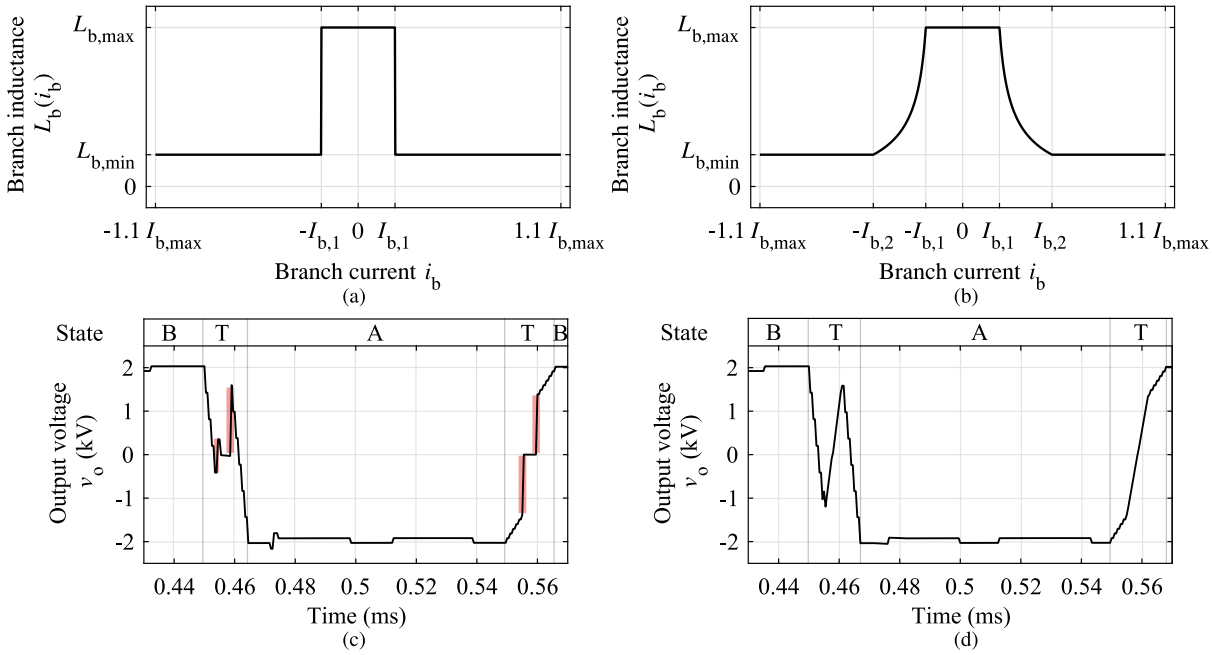

Fig. 3. Nonlinear branch inductors. (a) Straightforward characteristic of the inductance. (b) Extended branch inductance characteristic. (c) Example voltage waveform for the straightforward branch inductor characteristic. (d) Example voltage waveform for the extended branch inductor characteristic. State A, state B, and transition state are labeled by "A," "B," and "T," respectively. The problematic $\mathrm{d}v_\mathrm{o}/\mathrm{d}t$ is highlighted in (c).

equation in (4) for the following investigations, yielding

$$v_\mathrm{o} = -\frac{L_\mathrm{bB} - L_\mathrm{bA}}{L_\mathrm{bA} + L_\mathrm{bB}} \cdot \frac{V_\mathrm{i}}{2}. \tag{5}$$

Furthermore, the output voltage v_o is required to have a linear slope in time t with a constant gradient $\mathrm{d}v_\mathrm{o}/\mathrm{d}t$ and an offset $V_{\mathrm{o},0}$

$$v_\mathrm{o} = \frac{\mathrm{d}v_\mathrm{o}}{\mathrm{d}t} \cdot t + V_{\mathrm{o},0}. \tag{6}$$

Assuming that the branch inductor of Branch A conducts a high current and, thus, its inductance is $L_\mathrm{bA} = L_\mathrm{b,min}$, and that the inductance of the inductor in Branch B is being changed ($L_\mathrm{bB} = L_\mathrm{b}(t)$), the required inductance characteristic

$$L_\mathrm{b}(t) = L_\mathrm{b,min} \cdot \frac{\frac{V_\mathrm{i}}{2} - \frac{\mathrm{d}v_\mathrm{o}}{\mathrm{d}t} \cdot t}{\frac{V_\mathrm{i}}{2} + \frac{\mathrm{d}v_\mathrm{o}}{\mathrm{d}t} \cdot t} \tag{7}$$

can be determined using (5) and (6) as a function of time t with the gradient $\mathrm{d}v_\mathrm{o}/\mathrm{d}t$ as a parameter.

To express the branch inductance as a function of the branch current rather than as a function of time, the equation describing the behavior of the leg current

$$V_\mathrm{i} - v_\mathrm{bA} - v_\mathrm{bB} = (L_\mathrm{bA}(i_\mathrm{bA}) + L_\mathrm{bB}(i_\mathrm{bB})) \cdot \frac{\mathrm{d}i_\mathrm{leg}}{\mathrm{d}t} \tag{8}$$

can be used. Since the output current i_o is assumed not to change significantly during transition state, the change in the branch currents is caused solely by the change in the leg current: $\mathrm{d}i_\mathrm{b}/\mathrm{d}t \approx \mathrm{d}i_\mathrm{leg}/\mathrm{d}t$. By substituting the rest of the assumptions for the transition state ($v_\mathrm{bA} \approx v_\mathrm{bB} \approx V_\mathrm{i}$, $L_\mathrm{bA} = L_\mathrm{b,min}$, and $L_\mathrm{bB} = L_\mathrm{b}(t)$) into (8), the branch current waveform can be calculated by the following integral:

$$i_\mathrm{b}(t) = -\int_0^t \frac{V_\mathrm{i}}{L_\mathrm{b,min} + L_\mathrm{b}(t)}\,\mathrm{d}t + I_{\mathrm{b},1}. \tag{9}$$

Eliminating the time t from the solution for $L_\mathrm{b}(t)$ expressed in (7) and the solution for $i_\mathrm{b}(t)$ obtained from (9), the branch inductance $L_\mathrm{b}(i_\mathrm{b})$ can be determined according to (10) shown at the bottom of this page as a function of the branch current i_b.

The second branch-current switch-over value

$$I_{\mathrm{b},2} = I_{\mathrm{b},1} + \frac{1}{4} \cdot \frac{V_\mathrm{i}^2}{\frac{\mathrm{d}v_\mathrm{o}}{\mathrm{d}t} \cdot L_\mathrm{b,min}} \cdot \frac{L_\mathrm{b,max} - L_\mathrm{b,min}}{L_\mathrm{b,max} + L_\mathrm{b,min}} \cdot \left(1 - \frac{1}{2} \cdot \frac{L_\mathrm{b,max} - L_\mathrm{b,min}}{L_\mathrm{b,max} + L_\mathrm{b,min}}\right) \tag{11}$$

is determined using the second case from (10) for $L_\mathrm{b}(I_{\mathrm{b},2}) = L_\mathrm{b,min}$.

$$L_\mathrm{b}(i_\mathrm{b}) = \begin{cases} L_\mathrm{b,max} & |i_\mathrm{b}| < I_{\mathrm{b},1} \\ \sqrt{\frac{V_\mathrm{i}^2 \cdot L_\mathrm{b,min}}{2 \cdot \frac{\mathrm{d}v_\mathrm{o}}{\mathrm{d}t} \cdot (|i_\mathrm{b}| - I_{\mathrm{b},1}) + \frac{V_\mathrm{i}^2 \cdot L_\mathrm{b,min}}{(L_\mathrm{b,min} + L_\mathrm{b,max})^2}}} - L_\mathrm{b,min} & I_{\mathrm{b},2} > |I_\mathrm{b}| > I_{\mathrm{b},1} \\ L_\mathrm{b,min} & |i_\mathrm{b}| > I_{\mathrm{b},2} \end{cases} \tag{10}$$

The branch inductance characteristic described by (10) is demonstrated graphically in Fig. 3(b). In Fig. 3(d), a simulated output voltage waveform is plotted as an example for an MMC utilizing the proposed nonlinear inductors. Despite slightly lower undershoot in the output voltage, the figure demonstrates reduced $\mathrm{d}v/\mathrm{d}t$ of the output voltage between 0.455 and 0.46 ms and between 0.55 and 0.465 ms compared to that in Fig. 3(c). Hence, the derived inductor characteristic does not violate the advantage of low $\mathrm{d}v/\mathrm{d}t$ in the quasi-two-level PWM operation of MMCs.

V. Nonlinear Inductor Design

In this section, the practical design of the nonlinear inductor, specified in the previous section, is discussed.

A. Air-Gap Design

The nonlinear branch inductor can be designed for the specification described by (10) by adjusting the geometry of the air gap. In theory, there are three options to construct the air gap of a nonlinear inductor. The first option is a distributed air gap, provided by an adhesive in the magnetic powder material. A sloped air gap [23] represents the second option. Nevertheless, none of these is capable of providing two linear regions for the inductor with an abrupt change of inductance in between, as specified in Fig. 3(b). Only the third type, the stepped air gap, conforms to such a change in inductance. This type of inductor is based on air gaps with different heights inside the usual linear air gap to achieve the required inductance over current characteristic [24], [25]. Of course, the transfer from one step to the other can be realized with a slope of various forms to add another degree of freedom in the design. In general, this is possible, but not needed with respect to the aforementioned application, as shown based on the step air gap demonstrated in the following section. A common approach to stepped inductance design is to ignore the nonlinear properties of the material and consider only the area of each step that meets the saturation conditions. In this article, however, a more advanced approach modeling the continuous permeability that leads to more precise results is applied.

According to Kirchhof's law, used for equivalent magnetic circuits, the inductance of a simplified inductor with an air gap

$$L = N^2 \cdot \left(\frac{l_{\mathrm{core}}}{\mu_0 \cdot \mu_{\mathrm{r}} \cdot A_{\mathrm{core}}} + \frac{l_{\mathrm{air}}}{\mu_0 \cdot A_{\mathrm{core}}} \right)^{-1} \tag{12}$$

can be approximated as a function of number of turns N, the relative permeability of the core μ_{r}, and the equivalent area A_{core} of the air gap and the core. The length l_{core} is the effective length of the magnetic core and l_{air} is the air-gap length. Since the air-gap reluctance is usually significantly higher than the reluctance of the magnetic material, the magnetic resistance of the core can be neglected in the calculation. However, when the air gap is small enough (approx. $l_{\mathrm{air}} < \frac{l_{\mathrm{core}}}{\mu_{\mathrm{r}}}$), the magnetic voltage drop in the core becomes significant and the magnetic reluctance of the core should not be neglected anymore.

The 3-D diagram of the studied stepped inductor is depicted in Fig. 4. The air-gap length of the first step can be defined as a and the air-gap length of the second step as b. A_{c} is the platform area of the air gap of the first step and A_{e} is the platform area of the second step. The length of the magnetic circuit of the inductor is l_{e}.

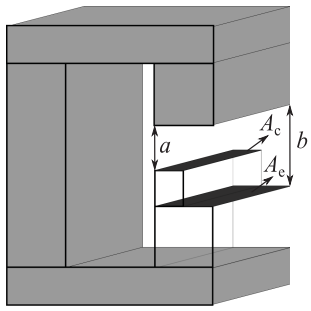

Fig. 4. 3-D diagram of the applied stepped inductor.

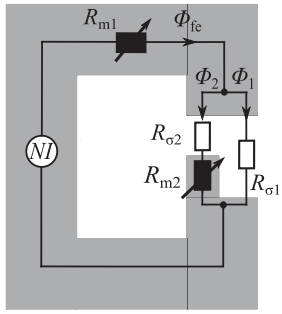

Fig. 5. Equivalent magnetic circuit diagram of the stepped inductor.

The equivalent magnetic circuit diagram of the stepped inductor is shown in Fig. 5. The corresponding reluctances can be expressed as

$$R_{\mathrm{m1}} = \frac{l_{\mathrm{e}} - b}{\mu_{\mathrm{r}} \cdot \mu_0 \cdot A_{\mathrm{e}}} \tag{13}$$

$$R_{\sigma 1} = \frac{b}{\mu_0 \cdot (A_{\mathrm{e}} - A_{\mathrm{c}})} \tag{14}$$

$$R_{\mathrm{m2}} = \frac{b - a}{\mu_{\mathrm{r}} \cdot \mu_0 \cdot A_{\mathrm{c}}} \tag{15}$$

$$R_{\sigma 2} = \frac{a}{\mu_0 \cdot A_{\mathrm{c}}}. \tag{16}$$

Reluctances R_{m1} and R_{m2} are associated with the core material. In order to describe the nonlinear properties of the core material, the permeability curve of the material can be replaced by a suitable fitting function [26].

Silicon steels are the preferable material that is widely used in low-frequency applications, due to their high-saturation magnetic flux density, generally up to 1.9 T, and relatively low cost. In order to further reduce the price of the core, rectangular bulk cores are often used. Nonlinear inductors are assembled from several of these bulk cores. The core can be laminated from laser-cut nonoriented electrical steels. Laser cutting technology has an accuracy of 0.01 mm, which makes it easy to shape the step air gap. The disadvantages of laser cutting are the thermal stress and the effect of lattice breakage on the magnetic

properties of the cut edges. In this article, however, the step part of the air gap is often saturated, therefore, the magnetic properties of the step part do not affect the inductor too much. Also, due to the presence of the steps, the area of the cutting edge of the magnetic column is reduced, so the impact of the cutting is further diminished. In [27]–[29], the effects of different cutting techniques on the magnetic properties were described qualitatively as well as quantitatively. Due to the inevitable air gap between the cores and their orientation in the magnetic circuit, the advantage of the oriented steel cannot be utilized, so the nonoriented steel M235-35 A is used for the calculations. The BH characteristic curve of M235-35 A can be obtained by measurement. In this article, the permeability curve of M235-35 A is represented by a three-term Gaussian function

$$\mu_{\mathrm{r}} = 0.01\,143 \cdot e^{-\left(\frac{B-0.4896}{0.3194}\right)^2} + 0.0199 \cdot e^{-\left(\frac{B+0.1824}{0.06\,545}\right)^2} + 0.0051 \cdot e^{-\left(\frac{B-0.8964}{0.2631}\right)^2}. \tag{17}$$

As shown in Fig. 5, the relationship between the magnetic fluxes ϕ_{fe}, ϕ_1, and ϕ_2 in the magnetic circuit is

$$\phi_{\mathrm{fe}} = \phi_1 + \phi_2 \tag{18}$$

with

$$\phi_1 = \frac{N \cdot i_{\mathrm{b}} - \phi_{\mathrm{fe}} \cdot R_{\sigma 1}}{R_{\mathrm{m2}}} \tag{19}$$

where the magnetic flux ϕ_{fe} can be obtained by integrating the LI curve of Fig. 3(b), which is defined by the application. Flux ϕ_2 is determined by the magnetic resistances R_{m1} and R_{m2}, which are nonlinear, and flux ϕ_1 passes through the linear reluctances and, thus, is linear. Its value can be obtained by subtracting flux ϕ_2 from the flux ϕ_{fe}. As a result, the magnetic flux density B_2 through R_{m2} is

$$B_2 = \frac{\phi_2}{A_{\mathrm{c}}}. \tag{20}$$

When the value of B_2 is substituted into (17), permeability at the working point at the R_{m2} branch is obtained. The magnetic flux density B_{e} in the R_{m1} branch is calculated directly from the magnetic flux ϕ_{fe} and cross-sectional area A_{e}. The corresponding inductance value for each operating point of current i_{b} can be obtained on the LI curve, the inverse of $\frac{N^2}{L_{\mathrm{b}}}$ are the total reluctance corresponding to each operating point. Eventually, according to Fig. 5, the magnetic circuit equation

$$R_{\mathrm{total}} = R_{\mathrm{m1}} + \frac{(R_{\mathrm{m2}} + R_{\sigma 2}) \cdot R_{\sigma 1}}{R_{\mathrm{m2}} + R_{\sigma 2} + R_{\sigma 1}} \tag{21}$$

can be derived. This equation consists of a total of five unknowns, therefore five working points on the LI curve are required. This set of equations can be solved by the least squares method. The initial values of the variables can be calculated using the traditional stepped design method.

B. Inductor Design Specification

The nonlinear inductor that is considered for the design example (and later for simulations) is selected to replace a linear inductor with branch inductance $\overline{L}_{\mathrm{b}} = 100\,\mu\mathrm{H}$. The minimum branch inductance, which was estimated as sufficient for the controller, was selected to be $L_{\mathrm{b,min}} = 30\,\mu\mathrm{H}$. Furthermore, the value $I_{\mathrm{b},1}$ was selected to be 50 A, which is sufficiently higher than the controlled currents during state A and state B. To achieve the same branch current ripples, the inductance value $L_{\mathrm{b,max}}$ is determined to be $L_{\mathrm{b,max}} = 170\,\mu\mathrm{H}$ according to (3). The value $I_{\mathrm{b},2}$ is 200 A, to maintain $\mathrm{d}v_{\mathrm{o}}/\mathrm{d}t = 400\,\frac{\mathrm{V}}{\mu\mathrm{s}}$.

TABLE I
RESULTS OF GEOMETRIC PARAMETERS OF STEPPED INDUCTOR

	Geometric parameters of calculation	Geometric parameters after numeric iteration with Maxwell	Error
Length a	1.3 mm	1.83 mm	-28 %
Length b	5 mm	5 mm	0 %
Area A_{c}	75 mm^2	108 mm^2	-30.5 %
Length l_{e}	300 mm	300 mm	0 %
Area A_{e}	300 mm^2	300 mm^2	0 %

C. Design Results and Further Iterations

The results of the calculation from Section V-A are presented in Table I. The resulting air gap has two steps: The first step has a cross-sectional area of $A_{\mathrm{c}} = 75$ mm^2 and a length of $a = 1.3$ mm. The second step has an area $A_{\mathrm{e}} = 300$ mm^2 and a length of $b = 5$ mm. The number of turns is $N = 30$.

The FEM simulation software Ansys Maxwell 2-D was used to validate the calculation results. The simulation results are shown in Fig. 6 as red curve.

Fig. 7 presents the design process for the nonlinear inductor. The calculations done in MathWorks MATLAB are presented in a dark grey box. The finite element simulation iterations are completed using Ansys Maxwell. The corresponding process is marked by a light grey box.

As shown in Fig. 6, the LI characteristic of the designed nonlinear inductor does not perfectly fit that according to (10) but gives a good starting point for further iterations based on numerical simulations. The reasons leading to this result include: First, as shown in Fig. 6, only five variables with clear geometric definitions are set, which also means that five working points on the LI characteristic curve are selected, which are then substituted back into (21). If the magnetic circuit diagram of the inductor is depicted in more detail, e.g., R_{m1} is replaced by three or more resistances, then the number of working points required in the calculation will increase. The more working points are selected, the more accurate the calculation will be. Second, due to the large range of currents, especially low inductance currents $I_{\mathrm{b},2}$ to $I_{\mathrm{b,max}}$ ranging from 200 to 500 A, more steps might be required. Third, the relatively large air-gap length of the nonlinear inductor causes an increased magnetic flux leakage in the proximity of the air gap. Viewed from the magnetic circuit, the flux leakage acts like a linear reluctance paralleled to the air gap. This leads to a reduction of the total reluctance, which increases the inductance.

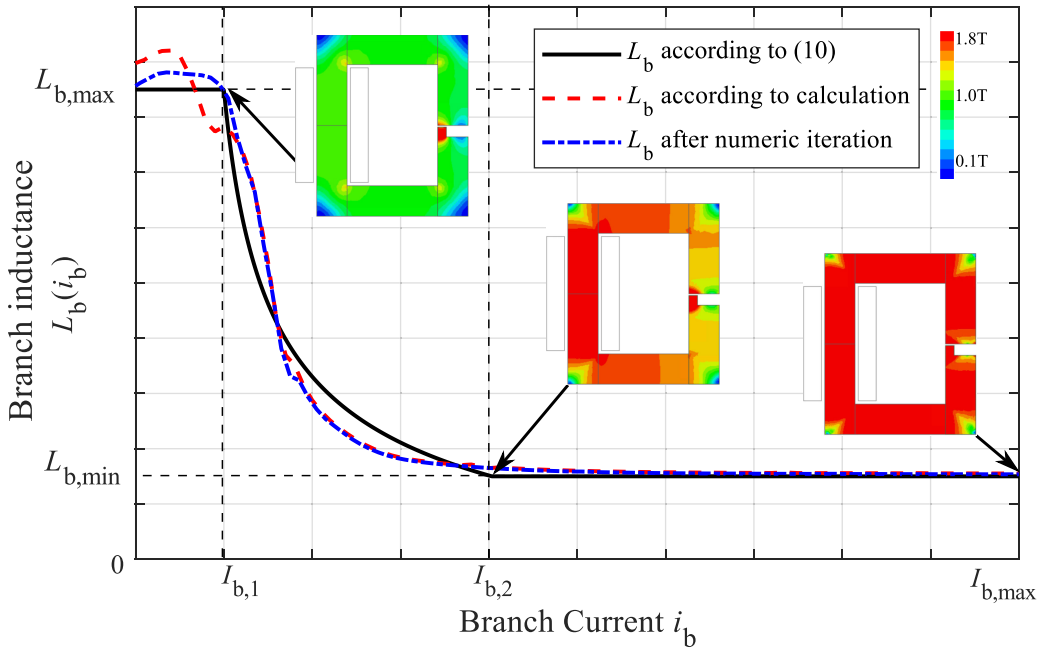

Fig. 6. Branch inductance $L_{\mathrm{b}}(i_{\mathrm{b}})$ characteristic of the designed nonlinear inductor obtained from FEM simulation of calculation result (red) and FEM simulation result after numeric iteration (blue) compared to the required characteristic described by (10). The pictures show the saturation state of the core for the different operating points is indicated by arrows. Design parameters: $\mathrm{d}v_{\mathrm{o}}/\mathrm{d}t = 400\ \frac{\mathrm{V}}{\mu\mathrm{s}}$, $L_{\mathrm{b,max}} = 170\,\mu\mathrm{H}$, $L_{\mathrm{b,min}} = 30\,\mu\mathrm{H}$, $I_{\mathrm{b},1} = 50$ A, $I_{\mathrm{b},2} = 200$ A, and $I_{\mathrm{b,max}} = 500$ A.

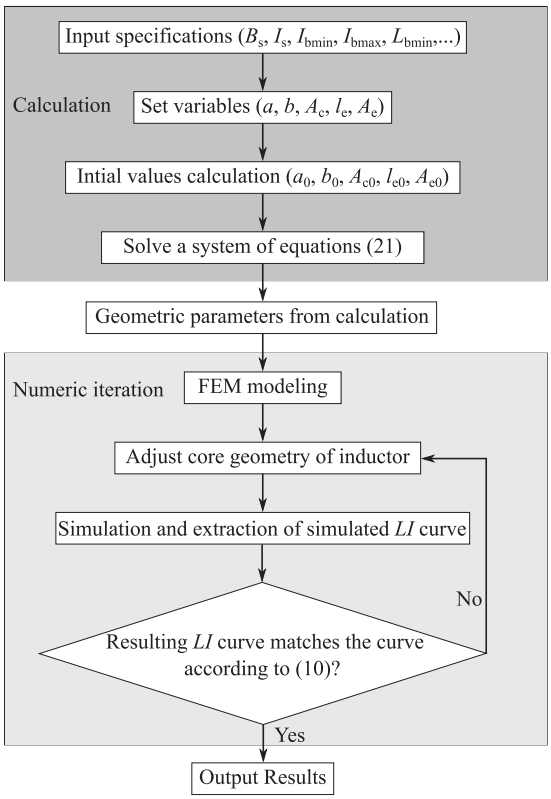

Fig. 7. Flowchart of the nonlinear inductor design with a calculation part (dark gray area) and an FEM simulation part (light gray area). The criterion for the evaluation of the resulting LI curve is selected based on the application and system simulations.

In order for the LI characteristics of the designed inductor to match Fig. 6, the inductor model in Maxwell must be adjusted. The second column in Table I lists the results of the geometric parameters after numerical iteration in Maxwell (light grey area in Fig. 7). The adjusted LI characteristic simulation result is represented by the blue curve in Fig. 6 together with the core saturation at three operation points. The third column of Table I lists the error between the results of the numerical iterations and the results of the direct calculations, as reference for the application of the presented method.

For a linear inductor design, core saturation has to be avoided because of the harmonics and distortion that can occur. In contrast, the mentioned nonlinear inductor needs to push the magnetic material to saturated state (see Fig. 6). In fact, the saturated region of the magnetic material is also a linear region in which the inductance is almost a constant, despite the large variation in current. Another possible effect of higher flux density in the step during state A is an increase in core loss. Fig. 8 presents the distribution of the core loss density without dc offset. As shown, the core loss is increased in the stepped part of the air gap to approximately 300 $\mathrm{kW/m^3}$.

Finally, it can be concluded that the 2-D FEM simulation confirmed the feasibility of the specified nonlinear inductor. The results from the FEM simulations are used later for the simulations of the quasi-two-level PWM-operated MMC. As already mentioned, also other smoother shapes or slopes between the steps could theoretically be implemented to improve the fit of the characteristics. Nevertheless, this further increases the complexity of the derivation and possibly even construction.

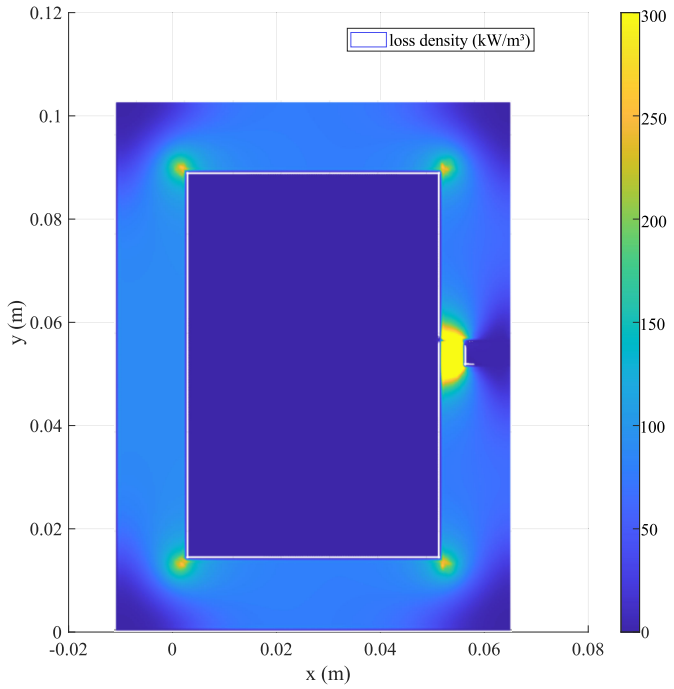

Fig. 8. Core loss density distribution map of the nonlinear inductor with current ripple $\triangle i_b = 35$ A and without dc bias. The 2-D transient finite element simulation provides the distribution of the flux density along with the BH characteristic of material. The loss density distribution is then calculated in MathWorks MATLAB using Steinmetz's equation without considering the saturation.

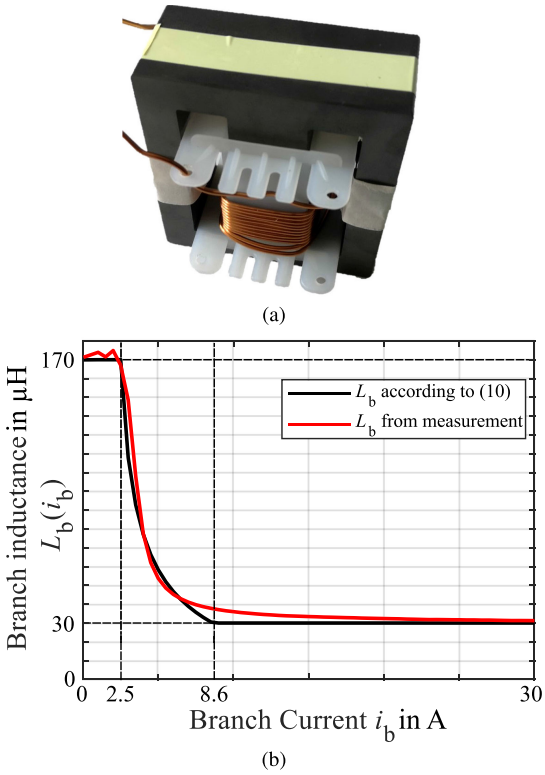

Fig. 9. Demonstrator of the nonlinear branch inductor used for measurements with downscaled MMC prototype: (a) photo and (b) measured $L_\mathrm{b}(i_\mathrm{b})$ characteristic. Design parameters: $\mathrm{d}v_\mathrm{o}/\mathrm{d}t = 30\,\frac{\mathrm{V}}{\mu\mathrm{s}}$, $L_\mathrm{b,max} = 170\,\mu\mathrm{H}$, $L_\mathrm{b,min} = 30\,\mu\mathrm{H}$, $I_\mathrm{b,1} = 2.5$ A, $I_\mathrm{b,2} = 8.6$ A, and $I_\mathrm{b,max} = 30$ A.

VI. Nonlinear Branch Inductor Demonstrator

To demonstrate the practical feasibility of the nonlinear inductance with a stepped air gap, a downscaled demonstrator was constructed [displayed in Fig. 9(a)]. Because of the lower inductor current ratings of the demonstrator, a standardized ferrite core could be applied to decrease the overall costs for the prototype. The stepped air gap was realized by inserting small ferrite blocks into the air gap. The measured characteristic in Fig. 9(b) demonstrates that the required characteristic can be fitted quite well. Furthermore, two of these inductor demonstrators are used later to experimentally validate the operation with a downscaled MMC prototype.

VII. Control Adjustment

The control approach from [9] has been applied to the investigated converter. Since the total leg inductance is almost constant during states A and B: $L_\mathrm{bA} + L_\mathrm{bB} = 2 \cdot \overline{L}_\mathrm{b}$ (assuming one branch current is greater than $I_{\mathrm{b},2}$ and one branch current is below $I_{\mathrm{b},1}$), the nonlinear inductors do not influence the dead-beat controller significantly. However, during the transition state, the leg inductance changes dynamically, and thus, the branch current has to be predicted in a different manner than in [9].

Instead of predicting the branch currents during the whole period of the transition state using only a single measured value captured at the beginning of the transition state, the corresponding branch current, which is predicted ($\tilde{i}_{\mathrm{b}x}$), is measured continuously and only the small part of the current that is added during frozen states is calculated predictively

$$\tilde{i}_{\mathrm{b}x}(k) = i_\mathrm{b}(k) + \frac{1}{2 \cdot \overline{L}_\mathrm{b}} \cdot \xi. \tag{22}$$

The variable ξ represents the voltage time-integral value applied to the leg inductor during the frozen state A or frozen state B. For further explanations of the control and frozen states, see [9].

It has to be noted that this change made to the control for operation in transition states increases the sensitivity of the current control performance to the bandwidth of the current sensors. Since the currents need to be measured precisely during the steep current changes present in transition states, a high sensor bandwidth becomes more important compared to the control for linear inductors from [9], where the currents are predicted.

VIII. Simulation Results

To evaluate the potential of the nonlinear inductors, a simulation of a three-phase quasi-two-level PWM-operated MMC was conducted. The simulation model was implemented in MathWorks Simulink. The physical part of the model was implemented in Plexim Plecs toolbox, including the nonlinear branch inductors, which were implemented using the "variable inductor" component from Plecs library. The characteristic of the nonlinear inductors was defined by a look-up table obtained from

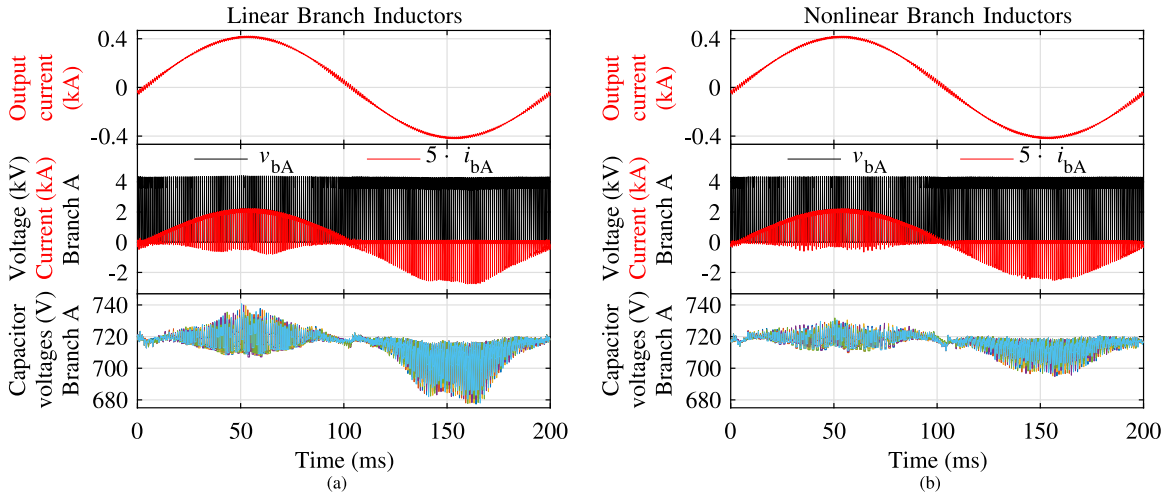

Fig. 10. Simulated waveforms of the first phase leg of quasi-two-level PWM-operated MMC with modulation index $M = 1.05$, carrier-based space-vector modulation: (a) with linear branch inductors ($L_b(i_b) = \overline{L}_b = 100\,\mu$H) and (b) with nonlinear branch inductors $L_b(i_b)$ according to Fig. 6.

TABLE II
CONVERTER PARAMETERS FOR SIMULATION

Input voltage	V_i	4 kV
Output current amplitude	$\hat{i}_o$	400 A
Modules per branch	n_{mpb}	6
Module capacitance	C_{mod}	200 µF
Capacitor voltage	V_C	720 V
PWM frequency	f_{PWM}	1 kHz
HF modulation frequency	f_{HF}	25 kHz
Switching delay time	T_d	1 µs
Load	$v_{o,s}$	0 V
	R_o	5 Ω
	L_o	15 mH
	f_o	5 Hz

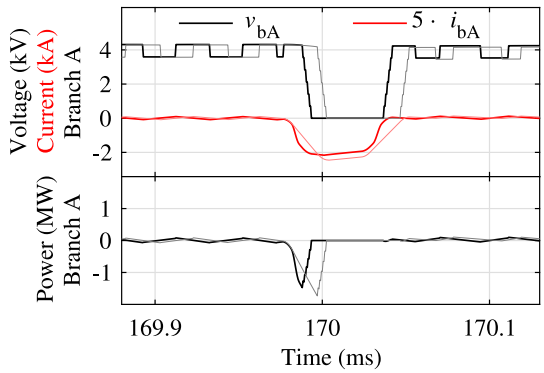

Fig. 11. Detailed comparison of waveforms from Fig. 10 for Branch A between the operation with nonlinear inductors (thick lines) and linear inductors (pale thin lines).

the FEM simulations presented in Section V-C. The converter and load parameters are listed in Table II.

Comparing the waveforms simulated over one output period for linear branch inductors in Fig. 10(a) and nonlinear branch inductors in Fig. 10(b), several properties can be stated, which are as follows.

1) The output current is practically not influenced by the choice of inductor type, since the load inductance L_o is significantly higher than the branch inductances.
2) The branch energy variation is significantly lower for nonlinear branch inductors, which can be seen by comparing the variations of the module capacitor voltages.
3) The peak values of branch currents are lower with nonlinear branch inductors, since the branch energies which must be compensated for during state A or B are lower as well.

Fig. 11 shows a detail of the waveforms of Branch A for an operation with nonlinear branch inductors (plotted with thick lines) and with linear inductors (plotted with pale thin lines). Although the branch current ripple is almost the same during state A, the branch current changes significantly faster from the (very low) positive value to the negative value during the transition state, and thus, the duration of the transition state is shorter. This leads to a shorter period of nonzero branch power, and thus, lower branch energy disturbance occurs.

Furthermore, the total branch energy variation

$$\Delta e_b = n_{mpb} \cdot \frac{1}{2} \cdot C_{mod} \cdot \left(V_{C,max}^2 - V_{C,min}^2\right) \qquad (23)$$

was evaluated for both quasi-two-level PWM operation of MMC with linear inductors [see Fig. 10(a)] and with nonlinear inductors [see Fig. 10(b)] using the maximum capacitor voltage value $V_{C,max}$ and the minimum capacitor voltage value $V_{C,min}$ captured during the operation. The comparison shows that the branch energy variation was reduced by 40% in the conducted simulation with nonlinear inductors ($\Delta e_b = 31.7$ J) compared to that of the MMC with linear inductors ($\Delta e_b = 54$ J). This enables an option to further reduce the size of the module capacitors, which is the main advantage of the operation with the nonlinear inductors. As (23) implies, the reduction of the branch energy variation by 40% enables a reduction of the module capacitance by 40% when the same module capacitor voltage boundaries ($V_{C,min}$ and $V_{C,max}$) are assumed.

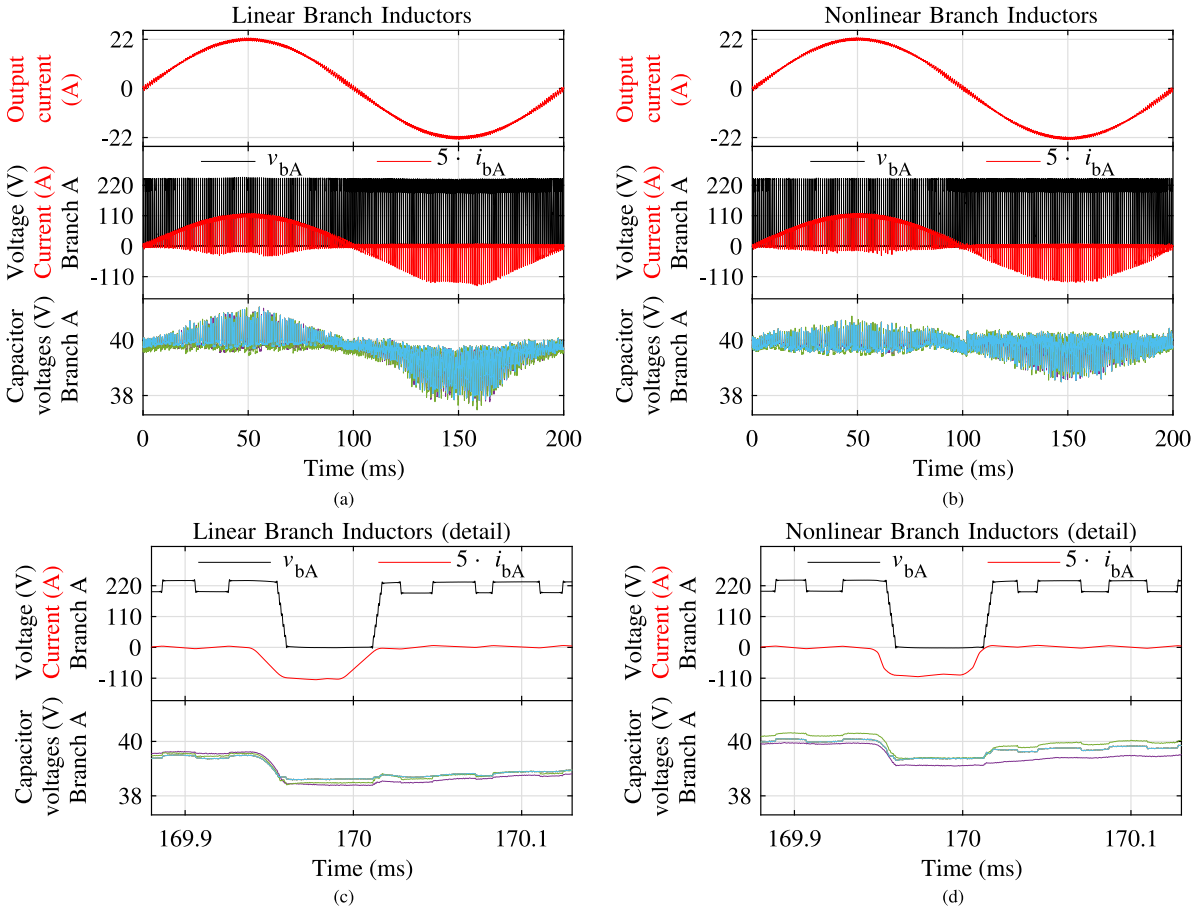

Fig. 12. Experimental waveforms of the first phase leg of quasi-two-level PWM-operated MMC with modulation index $M = 1.05$, carrier-based space-vector modulation: (a) with linear branch inductors ($L_\mathrm{b}(i_\mathrm{b}) = \overline{L}_\mathrm{b} = 100\,\mu\mathrm{H}$) and (b) with nonlinear branch inductors shown in Fig. 9; (c) and (d) detailed view of (a) and (b), respectively. The waveforms were captured by an eight-channel oscilloscope and filtered by an 1 MHz low-pass filter.

IX. Experimental Validation

The simulation results were validated using a downscaled converter prototype. The prototype is scaled down in both currents and voltages by a factor of 18. Hence, the converter is rated for the input voltage $V_\mathrm{i} = 220\,\mathrm{V}$ and the output current amplitude $\hat{i}_\mathrm{o} = 22\,\mathrm{A}$. The module capacitor voltage is controlled to $V_C = 40\,\mathrm{V}$. The rest of the parameters is identical to those from Table II. The details regarding the experimental test setup are presented in [8] and [9].

The experimental waveforms captured with the linear inductors [see Fig. 12(a)] and with the nonlinear inductor demonstrators [see Fig. 12(b)] are in good agreement with the simulated waveforms displayed in Fig. 10(a) and (b), respectively. Observing the experimental waveforms, the same advantages can be stated as for the simulated waveforms, i.e., slightly lower branch currents and significantly lower module capacitor voltage variation.

Fig. 12(c) and (d) shows the detailed view of the experimental waveforms from Fig. 12(a) and (b), respectively. Similarly as in simulations, these figures clearly demonstrate that branch current is changed significantly faster when nonlinear inductors are employed. As a consequence, the module capacitor voltage disturbance (the branch energy disturbance) is observably lower.

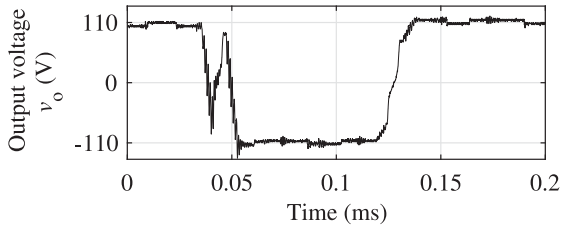

Fig. 13. Experimental output voltage waveform of the MMC with nonlinear branch inductors shown in Fig. 9.

In Fig. 13, the measured output voltage waveform of quasi-two-level PWM operation with nonlinear inductors is shown. In the figure, a limited $\mathrm{d}v_\mathrm{o}/\mathrm{d}t$ of large voltage steps can be recognized. Furthermore, the waveform matches the theoretical one, plotted in Fig. 3(d), quite well.

X. Conclusion

In this article, an application of nonlinear branch inductors for quasi-two-level PWM-operated MMCs, suitable for drive applications, has been proposed. The nonlinear inductors, the specification of which has been derived in this article, proved to have the potential to significantly reduce the module capacitance without increasing the $\mathrm{d}v/\mathrm{d}t$ of the output voltage. FEM simulations and experiments with the inductor demonstrator validated the feasibility of the proposed nonlinear branch inductor design, featuring a stepped air gap.

In the future research, the influence of the design parameters, such as the values $I_{\mathrm{b},1}$ and $L_{\mathrm{b,min}}$, on the branch energy variation should be investigated analytically in more detail.

References

[1] J. Kucka, S. Lin, J. Friebe, and A. Mertens, "Quasi-two-level PWM-operated modular multilevel converter with non-linear branch inductors," in *Proc. Eur. Conf. Power Electron. Appl.*, Sep. 2019, pp. 1–10.

[2] A. Lesnicar and R. Marquardt, "An innovative modular multilevel converter topology suitable for a wide power range," in *Proc. IEEE Bologna Power Tech Conf. Proc.*, Jun. 2003, vol. 3, pp. 1–6.

[3] M. Spichartz, V. Staudt, and A. Steimel, "Modular multilevel converter for propulsion system of electric ships," in *Proc. IEEE Elect. Ship Technol. Symp.*, Apr. 2013, pp. 237–242.

[4] A. J. Korn, M. Winkelnkemper, and P. Steimer, "Low output frequency operation of the modular multi-level converter," in *Proc. IEEE Energy Convers. Congr. Expo.*, Sep. 2010, pp. 3993–3997.

[5] A. Antonopoulos, L. Ängquist, S. Norrga, K. Ilves, L. Harnefors, and H. P. Nee, "Modular multilevel converter ac motor drives with constant torque from zero to nominal speed," *IEEE Trans. Ind. Appl.*, vol. 50, no. 3, pp. 1982–1993, May 2014.

[6] A. Mertens and J. Kucka, "Quasi two-level PWM operation of an MMC phase leg with reduced module capacitance," *IEEE Trans. Power Electron.*, vol. 31, no. 10, pp. 6765–6769, Oct. 2016.

[7] J. Kucka and A. Mertens, "Control for quasi two-level PWM operation of modular multilevel converter," in *Proc. IEEE 25th Int. Symp. Ind. Electron.*, Jun. 2016, pp. 448–453.

[8] J. Kucka, "Quasi-two-level PWM operation for modular multilevel converters: Implementation, analysis, and application to medium-voltage drives," Ph.D. dissertation, Dept. Elect. Eng. Comput. Sci., Leibniz University Hannover, Germany, 2019.

[9] J. Kucka and A. Mertens, "Improved current control for a quasi-two-level PWM-operated modular multilevel converter," *IEEE Trans. Power Electron.*, vol. 35, no. 7, pp. 6842–6853, Jul. 2020.

[10] J. Kucka and A. Mertens, "Common-mode voltage injection techniques for quasi-two-level PWM-operated modular multilevel converters," *IEEJ J. Ind. Appl.*, vol. 8, no. 2, pp. 287–294, 2019.

[11] C. Wang, K. Wang, Z. Zheng, and Y. Li, "A new control strategy for modular multilevel converter operating in quasi two-level PWM mode," in *Proc. Int. Power Electron. Conf.*, May 2018, pp. 2386–2392.

[12] X. Gao, W. Tian, Z. Zhang, and R. Kennel, "Model predictive control with extrapolation strategy for the arm current commutation control of modular multilevel converter operating in quasi two-level mode," in *Proc. 10th Int. Conf. Power Electron. ECCE Asia*, May 2019, pp. 1–6.

[13] G. P. Adam, S. J. Finney, A. M. Massoud, and B. W. Williams, "Capacitor balance issues of the diode-clamped multilevel inverter operated in a quasi two-state mode," *IEEE Trans. Ind. Electron.*, vol. 55, no. 8, pp. 3088–3099, Aug. 2008.

[14] G. P. Adam, S. J. Finney, O. Ojo, and B. W. Williams, "Quasi-two-level and three-level operation of a diode-clamped multilevel inverter using space vector modulation," *IET Power Electron.*, vol. 5, no. 5, pp. 542–551, May 2012.

[15] I. A. Gowaid, G. P. Adam, A. M. Massoud, S. Ahmed, D. Holliday, and B. W. Williams, "Quasi two-level operation of modular multilevel converter for use in a high-power dc transformer with dc fault isolation capability," *IEEE Trans. Power Electron.*, vol. 30, no. 1, pp. 108–123, Jan. 2015.

[16] I. A. Gowaid, G. P. Adam, S. Ahmed, D. Holliday, and B. W. Williams, "Analysis and design of a modular multilevel converter with trapezoidal modulation for medium and high voltage dc-dc transformers," *IEEE Trans. Power Electron.*, vol. 30, no. 10, pp. 5439–5457, Oct. 2015.

[17] C. Sun, J. Zhang, Y. Chang, G. Shi, and X. Cai, "Wide voltage range operation of isolated modular multilevel dc-dc converter," in *Proc. 41st Annu. Conf. IEEE Ind. Electron. Soc.*, Nov. 2015, pp. 4953–4958.

[18] M. S. Diab, G. P. Adam, B. W. Williams, A. M. Massoud, and S. Ahmed, "Quasi two-level PWM operation of a nine-arm modular multilevel converter for six-phase medium-voltage motor drives," in *Proc. IEEE Appl. Power Electron. Conf. Expo.*, Mar. 2018, pp. 1641–1648.

[19] X. Wei, S. Lu, X. Deng, and S. Li, "A new quasi three-level hybrid modular multilevel converter," in *Proc. IEEE Int. Power Electron. Appl. Conf. Expo.*, Nov. 2018, pp. 1–6.

[20] J. Kucka and A. Mertens, "Designing a passively damped quasi-two-level-operated modular multilevel converter for drive applications," *IEEE Access*, vol. 8, pp. 80218–80232, 2020.

[21] M. Hagiwara and H. Akagi, "Control and experiment of pulsewidth-modulated modular multilevel converters," *IEEE Trans. Power Electron.*, vol. 24, no. 7, pp. 1737–1746, Jul. 2009.

[22] J. Kolb, F. Kammerer, and M. Braun, "Dimensioning and design of a modular multilevel converter for drive applications," in *Proc. 15th Int. Power Electron. Motion Control Conf.*, Sep. 2012, pp. LS1a-1.1-1–LS1a-1.1-8.

[23] W. Wolfle, W. G. Hurley, and S. Arnold, "Power factor correction for ac-dc converters with cost effective inductive filtering," in *Proc. IEEE 31st Annu. Power Electron. Specialists Conf. Proc.*, Jun. 2000, vol. 1, pp. 332–337.

[24] E. Stenglein, D. Kuebrich, and M. Albach, "Analytical calculation of the current depending inductance of a stepped air gap inductor," in *Proc. 18th Eur. Conf. Power Electron. Appl.*, Sep. 2016, pp. 1–10.

[25] J. Sun, M. Xu, Y. Ren, and F. C. Lee, "Light-load efficiency improvement for buck voltage regulators," *IEEE Trans. Power Electron.*, vol. 24, no. 3, pp. 742–751, Mar. 2009.

[26] M. Luo, D. Dujic, and J. Allmeling, "Modeling frequency independent hysteresis effects of ferrite core materials using permeance–capacitance analogy for system-level circuit simulations," *IEEE Trans. Power Electron.*, vol. 33, no. 12, pp. 10055–10070, Dec. 2018.

[27] M. Bali and A. Muetze, "The degradation depth of electrical steel sheets due to mechanical and laser cutting," in *Proc. IEEE 11th Int. Symp. Diagnostics Elect. Mach., Power Electron. Drives*, 2017, pp. 544–549.

[28] V. M. Paltanea, G. Paltanea, and H. Gavrila, "Some important effects of the water jet and laser cutting methods on the magnetic properties of the non-oriented silicon iron sheets," in *Proc. 9th Int. Symp. Adv. Topics Elect. Eng.*, 2015, pp. 452–455.

[29] V. Manescu, G. Paltanea, H. Gavrila, and I. Peter, "The influence of punching and laser cutting technologies on the magnetic properties of non-oriented silicon iron steels," in *Proc. Int. Symp. Fundam. Elect. Eng.*, 2014, pp. 1–4.

Jakub Kucka (Member, IEEE) received the bachelor's and master's degrees in electrical engineering from Czech Technical University, Prague, Czech Republic, in 2012 and 2014, respectively, and the Dr.-Ing. (Ph.D.) degree from Leibniz University Hannover, Hannover, Germany, in 2019.

From 2014 to 2019, he was a Research Associate with the Institute for Drive Systems and Power Electronics, Leibniz University Hannover. Since 2020, he has been a Postdoctoral Researcher with the Power Electronics Laboratory, EPFL, Lausanne, Switzerland. He has authored more than 20 scientific publications, one tutorial, and filed three patent applications. His research interests include modular multilevel converters, converter control and design, and resonant converter topologies suitable for high-power dc applications.

Dr. Kucka was the recipient of EPE Outstanding Young Member Award in 2020.

Siqi Lin was born in Fuzhou, China, in 1990. He received the B.Sc. degree in electrical engineering from Sanxia University, Yichang, China, in 2013, and the M.Sc. degree from the University of Kassel, Kassel, Germany, in 2018.

Since 2018, he has been a Research Assistant with the Institute for Drive Systems and Power Electronics, Leibniz University Hannover, Hannover, Germany. His current research interests include core loss study and design optimization of magnetic components for high-frequency power conversion.

Jens Friebe (Member, IEEE) was born in Göttingen, Germany. He received the B.Sc., M.Sc., and Dr.-Ing. degrees in electrical engineering from the University of Kassel, Kassel, Germany, in 2008, 2009 and 2014, respectively.

He has been responsible for the research area of passive components in power electronics with the Institute for Drive Systems and Power Electronics, Leibniz University Hannover, Hannover, Germany, since January 2018. Before that, he was with SMA Solar Technology, Niestetal, Germany, for more than 13 years, in the field of PV-inverter topologies, wide bandgap semiconductors, magnetic components, control strategies for high switching frequencies, and power electronics packaging. He invented more than 30 granted patents in the field of power electronics.

Axel Mertens (Senior Member, IEEE) received the Dipl.-Ing. and Dr.-Ing. (Ph.D.) degrees from RWTH Aachen University, Aachen, Germany, in 1987 and 1992, respectively.

In 1989, he was a Visiting Scholar with the University of Wisconsin–Madison, Madison, WI, USA. From 1993 to 2004, he was with Siemens AG in Erlangen and Nürnberg, Germany, with responsibilities for the control of large drives, including a variety of converter topologies, and for a product range of medium voltage inverters. In 2004, he was appointed a Professor for power electronics and drives with Leibniz University Hannover, Hannover, Germany. He served as the Department Chair with the Department of Electrical Engineering and Computer Science and as a Spokesman of the Energy Research Center LiFE 2050, Leibniz University Hannover. In addition to his academic duties, he had responsibilities within Fraunhofer IFAM, Bremen, Germany, and currently within Fraunhofer IEE, Kassel, Germany. He has authored or coauthored about 150 scientific papers. His research interests include the application of power semiconductor devices, design of power electronic circuits and systems, and control of power converters and drives. Applications focus on automotive applications, energy, and industrial drives. Outstanding research contributions include applications of WBG devices in e-mobility, control and topologies of modular multilevel converters, monitoring of power electronic devices, and fast self-sensing control of electric machines.

Prof. Mertens served as a Chairman of the IEEE Joint IAS/PELS/IES German Chapter and is an Associate Editor for the IEEE TRANSACTIONS ON POWER ELECTRONICS. Since 2019, he has been a member of the PELS AdCom. As the Head of the Department of Power Electronics of the German VDE-ETG, he chaired several national conferences in the field of power electronics.